Synthesis and Characterization of Methylammonium Lead Tri-Bromide Perovskites Thin Films by Sequential Physical Vapor Deposition

J. N. Fru[a], N. Nombona[b], M. Diale[a*]

[a]*Department of Physics, University of Pretoria, Private Bag X20, Hatfield 0028, South Africa*

[b]*Department of Chemistry, University of Pretoria, Private Bag X20, Hatfield 0028, South Africa*

Correspondence author's email and phone number: mmantsae.diale@up.ac.za, +27824519290

Abstract

Methylammonium lead tri-bromide ($MAPbBr_3$) thin films were grown by sequential physical vapor deposition of lead(II)bromide and methylammonium bromide (MABr). X-ray diffractograms confirmed the cubic $MAPbBr_3$ structure with $Pm\overline{3}m$ space group. UV-Vis spectra revealed a red shift in absorption onset from 540 to 550 nm as the thickness of MABr increased. An optimum band gap of 2.28 eV was obtain from band gap Tauc Plots. Field emission scanning electron micrographs showed large pin-hole-free and densely packed grains with average grain size that increased from 217 to 302 nm with increase in MABr thickness. Analysis of dark current-voltage characteristics of Au/$MAPbBr_3$/FTO devices revealed ohmic behavior at low voltages and trap-limited space charge limited current at high voltages. The carrier mobility increased from 1.89×10^{-2} to 1.08×10^{-1} $cm^2\ V^{-1}\ s^{-1}$ while trap density decreased from 1.89×10^{16} to 1.40×10^{16} cm^{-3} as the thickness of MABr increased.

Keywords: Methylammonium lead tri-bromide; sequential physical vapor deposition; methylammonium bromide; lead(II)bromide; ohmic behaviour; space charge limited current.

1 Introduction

Organic-inorganic perovskites (OIPs) semiconductors have excellent optoelectronic properties such as low exciton binding energy [1], long carrier diffusion length [2], large optical absorption range [3], tuneable bandgap [4], low defect density [5], self-doping [6], ambipolar charge carrier transport [7], and low phonon energy [8]. In addition, they have cheap and easy preparation methods, which include spin coating [9], spray pyrolysis [10], dip coating [11], physical vapor deposition [12], chemical vapor deposition [13], RF-magnetron sputtering [14], inkjet printing [15] and electrodeposition [16]. Furthermore, OIPs are suitable for several applications including photovoltaics [17], light emitting diodes [18], lasers [19], gas sensors [20], solar batteries [21], memory devices [22] and photo-detectors [23]. Among these, perovskite solar cells (PSCs) have shown increased power conversion efficiencies (PCE) ranging from 3.8 (2009) [24] to 23.7 % (2018) [25], making them the fastest emerging photovoltaic technology. This record closely matches that of commercially available monocrystalline silicon (26.7 %) and surpasses that of Cu(In, Ga)Se_2 (CIGS) (22.9 %) thin film solar cells [26]. However, the problem of instability is a major drawback towards commercialization. For example, the lifetime of PSCs is limited to 3000 hours [27], whereas commercially available photovoltaics have a lifetime of 25 years. The stability of PSCs depend on the durability of OIPs active layer, which is affected by moisture [28], high temperatures and thermal cycling [29], UV-radiation [30], structure [31], reaction with diffused metal electrodes [32], film quality [33] and stoichiometry [34]. Structural stability and performance of OIPs depend on the value of the Goldschmidt tolerance factor [35] which must be between 0.8 and 1 for stable OIPs. Likewise, stability is also affected by the reaction between metal electrodes and diffused OIPs materials. Ming et al. [32] proved that Au, Ag and Cu, when used as electrodes, diffused easily into OIPs layer at room temperature and promoted degradation. They also predicted that the presence of Au in methylammonium lead tri-iodide ($MAPbI_3$) caused the formation of deep level traps, resulting in nonradiative recombination. Similarly, halides from the decomposition of perovskites diffused through the hole transport layer, attacked the electrodes and caused corrosion [36]. The correct stoichiometry is also essential to achieve long term stability. *Schmidt et al*. [34] used secondary electron hyperspectral imaging (SEHI) to demonstrate that non-stoichiometric grains of OIPs degraded faster than stoichiometric ones. In addition, high temperatures and thermal cycling also lead to instability. Sheikh et al. [29] studied the effect of high temperatures and thermal cycling on m-TiO_2/$CH_3NH_3PbI_{3-x}Cl_x$/spiro-OMeTAD structure. They observed that thermal cycling caused degradation of short circuit current (I_{sc}) and fill factor, while high temperatures reduced I_{sc} and open circuit voltage (V_{oc}) and concluded that thermal cycling and high temperatures caused irreversible deterioration of PSCs due to accelerated recombination. In addition, grain boundaries and residual

strain reduce performance and cause degradation. *Yang et al.* [37] proved that grain boundaries were actively involved in the degradation of performance of PSCs. They stated that this can be reduced by producing quality films with large grains and few grain boundaries. *Zhao et al.* [38] showed that stability of OIPs film depended on residual strain, which increased the rate of degradation. Large densely packed grains and residual strain are instrumental for stability and high-performance of PSCs [39]. Such stable films can be prepared via high quality methods like physical vapor deposition (PVD).

Research on OIPs has focused on methylammonium lead tri-iodide ($MAPbI_3$) perovskites because they absorb in the entire visible range resulting in high PCE. However, methylammonium lead tri-bromide ($MAPbBr_3$) thin films have a large band gap, which results in high V_{oc} and high external quantum efficiency (EQE) [40]. This makes them suitable materials for application in tandem PSCs [41] and light emitting diodes [42]. In addition, high PCE (11.40 %) and stable PSCs have been achieved with $MAPbBr_3$ quantum dots [9]. Most reports on $MAPbBr_3$ perovskites devices have utilised solution-based synthetic methods. For example, the pioneering report on the use of OIPs as light sensitizers in dye sensitized solar cells by *Kijoma et al*. [24] was based on $MAPbBr_3$ and $MAPbI_3$ prepared by solution-based method (spin coating). The PSCs that utilized $MAPbBr_3$ showed high V_{oc} (0.96 V), high EQE (65 %) and low PCE (3.8 %). Similarly, *Jäckle et al*. [43] synthesized $MAPbBr_3$ thin film by spin coating equimolar solution of PbBr and MABr for tuneable green lasing. Partial-vapor methods have also been applied for synthesis of $MAPbBr_3$. For example, *Sheng et al*. [40] reported the preparation of $MAPbBr_3$ thin films by vapor-assisted deposition. Their approach included the deposition of a solution of $PbBr_2$ by spin coating followed by treatment of the deposited film with MABr vapor at 150˚C for 10 minutes. They achieved films with long carrier diffusion length exceeding 1 μm and PSCs with PCE of 8.7 % and V_{oc} of 1.45 V. Presently, chemical vapour deposition (CVD) is the only vapor method that has been used for the preparation of $MAPbBr_3$. *Leyden et al*. [42] synthesized $MAPbBr_3$ by CVD for light emitting diode and achieved luminescence of 560 cd/m^2. PVD is an environmentally friendly, scalable and reproducible method. It is applied in laboratories and industries for the deposition of high-quality thin films [44] and produces high purity films which do not depend on solubility of precursors in particular solvents. In addition, it can be applied on a variety of substrates [45]. PVD has the potential to improve stability by enhancing stoichiometry and quality of the OIPs thin films. Most attempts to prepare OIPs by PVD have focused on using separate source co-evaporation and single source evaporation, which are difficult to control and reproduce. This is because the rate of deposition fluctuates due to the small molecular weights of the powdered precursors, resulting in random collisions of vapor with air molecules in the chamber [46]. On the other hand, sequential physical vapor deposition (SPVD) can be controlled and is reproducible since the thickness can be accurately monitored by a quartz crystal monitor. However, SPVD has been rarely exploited for the synthesis of OIPs. *Jung et al.* [47] synthesized lead-free methylammonium tin tri-iodide ($MASnI_3$) by both SPVD and co-evaporation. They realized that the sequential physical vapor deposited films were more efficient than co-evaporated ones.

In this work, we have synthesized $MAPbBr_3$ thin films by SPVD of $PbBr_2$ and MABr single layers. The structure, surface morphology, visible light absorption, charge carrier mobility, trap density and photoelectrical properties of the synthesized films are analysed and optimized by varying the thickness of MABr. The Williamson-Hall (W-H) plot is used to determine the inseparable contribution of crystallite size and micro-strain to X-ray line broadening. The optical band gap is evaluated using the direct band gap Tauc-plot of the absorption spectra and the Mott-Gurney theory is applied to determine the charge transport properties (carrier mobility and trap densities). To the best of our knowledge, the synthesis of $MAPbBr_3$ by all-PVD methods and calculation of charge carrier mobility of polycrystalline $MAPbBr_3$ thin films using the Mott-Gurney theory are yet to be reported. Our approach involves only thickness control by a quartz crystal monitor and can be reproduced. This method is fast, scalable, repeatable, controllable and leads into quality $MAPbBr_3$ thin films for stable and high-performance solar cells.

2 Experimental details

Figure 1 shows the schematic diagram for growing $MAPbBr_3$ by SPVD. Fluorine doped tin oxide (FTO) substrates were trimmed into 15 mm x 20 mm, cleaned sequentially in acetone, isopropanol and deionized water and dried in nitrogen gas. The substrates were mounted on a sample holder and loaded into resistive evaporator. $PbBr_2$ (99.9 %) and MABr (98%) powders obtained from Sigma Aldrich were used as received. The powders were placed into separate boron nitride crucibles, labelled C_1 and C_2, in the chamber before evacuation. First, $PbBr_2$ film was deposited followed by the deposition of MABr. The substrate was at room temperature before the deposition. During the deposition of the MABr on the $PbBr_2$, the heat generated from heating the crucible raises the temperature of the substrate to 95 ˚C. Complete crystallisation was achieved by annealing the as-deposited sample in air at 100˚C for 10

minutes. The thickness of $PbBr_2$ was kept constant at 100 nm while that of MABr was varied from 300 to 500 nm in steps of 100 nm. A quartz crystal monitor was used to measure the thickness of the deposited film. For the fabrication of devices for dark current-voltage (*I-V*) analysis, one end of the FTO substrate was covered with aluminium foil to serve as the ohmic contact. $MAPbBr_3$ was then grown on the substrate, followed by deposition of gold using 0.6 mm diameter circular mask. Devices for Photoelectrical testing were fabricated using a finger-like mask that allowed enough light to reach the $MAPbBr_3$. The experiment was repeated on glass as substrate and for the 500 nm thick MABr sample with annealing time varied from 0 to 60 minutes.

Structural properties of the thin films were assessed by the Bruker D2-Phaser X-ray diffractometer (XRD) using Cu Kα radiation with wavelength of 0.15405 nm. The angle between the incident and diffracted rays, 2θ was varied from 10˚ to 50˚ in steps of 0.05˚. The measured diffractograms were used to determine the structure, crystallinity, crystal size, residual strain and dislocation density of the films. The morphology of the film was studied by Field Emission Scanning Electron Microscopy (FE-SEM, Zeiss Crossbeam 540). Grain size analysis was done on the FE-SEM micrographs following the American standard for testing materials (ASTM) with the help of image J software. The optical absorption spectra of the films were measured by CARY 100 BIO UV-Vis spectrometer with wavelength of incident light ranging from 400 to 800 nm. The current-voltage (I-V) measurements of the devices were evaluated by B2900 SMU. Light I-V measurement were performed with help of a Model 91150V Solar Simulator with solar output conditions of 1000 W/m^2 at 25 and AM1 reference spectral filtering. The thickness of the annealed $MAPbBr_3$ film was calculated from 1,

$$t = \frac{m}{\rho A} \qquad 1$$

where t is film thickness, ρ is density of $MAPbBr_3$ (3.83 g cm^{-3}) [42], A is surface area of substrate, m is the mass of the film, obtained by subtracting the mass of substrate from the mass of the thin film plus substrate.

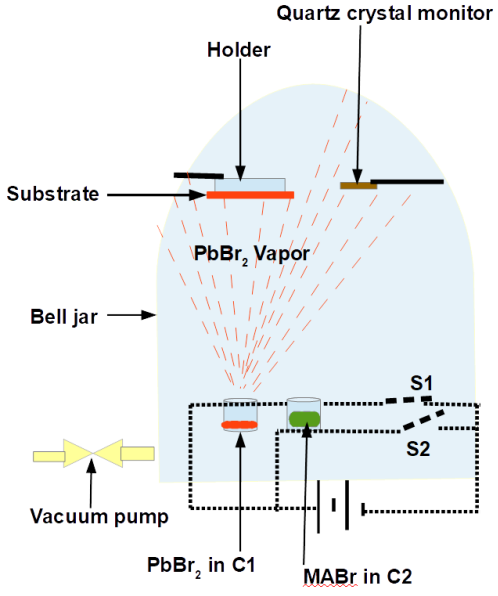

Figure 1: Experimental set-up for SPVD of $MAPbBr_3$ thin film

3 Results and discussion

3.1 Structural properties

Figure 2a shows the XRD spectra of $MAPbBr_3$ thin films on FTO for different MABr thickness. All the diffractograms showed sharp peaks depicting high crystallinity. The measured 2θ peaks occurred at 14.95˚, 21.14˚, 23.88 ˚, 26.54˚, 30.13˚, 33.73˚, 37.67˚, 43.12˚, 45.86˚ and 48.47˚. The peak positions indicate the structure and symmetry of contributing phase. This closely agrees with reports for cubic $MAPbBr_3$ single crystals with $Pm\bar{3}m$ space group [48–50]. The diffraction directions at 14.95˚, 21.14˚, 26.54˚, 30.13˚, 33.73˚, 37.67˚, 43.12˚, 45.86˚ and 48.47˚ are attributed to (100), (110), (111), (200), (210), (211), (220), (300), and (310) diffraction planes respectively. In addition, the results show a peak at 23.88˚, which does not occur on previous diffractograms for the single crystals. This peak was initially indexed by JCPDS card file number 31-0679 to $PbBr_2$ and supported by the XRD spectrum of $PbBr_2$ powder shown in Figure S1 (Supporting information). However, the effect of increasing annealing time and thickness of MABr on the intensity of the peak is monitored to further confirm its origin. The intensity is observed to increase, like those of the other peaks corresponding to $MAPbBr_3$, with increase in the thickness of MABr as shown by Figure 2a. Increase in the thickness of MABr increases the number of carbons, hydrogen and bromide atoms. This may cause the Wyckoff positions for the space group to be occupied by the required number of atoms leading to high structure factor and consequently high intensity peaks. Another reason for increase in intensities could be due to increase in the number of planes oriented in given directions which increase the multiplicity factor and consequently the peak intensities. Increasing the annealing time for 500 nm thick MABr thin film reduce both the intensity of the extra peak and that of the prominent (100) peak for $MAPbBr_3$ as shown in Figure S1 (supporting information). The intensity of the prominent (100) plane decreases for the first 40 minutes before increasing again as the time increased to 60 mins. This indicates that the prominent (100) peak of $MAPbBr_3$ and the peak at 23.88˚ show similar response to increase in annealing time. These effects of increasing annealing time and thickness of MABr on the intensity of the peak points to the possibility that the extra peak may be one of the characteristic peaks of $MAPbBr_3$ polycrystalline thin film on FTO and glass substrates. This peak may not be observed on the $MAPbBr_3$ single crystal spectra because their diffractograms do not depend on substrate, but crystallographic directions of polycrystalline thin films depend on several factors including type of substrate, method of deposition and growth conditions. Decrease in intensity of the (100) peak with increase in annealing time shows decrease in crystallinity, which may point out that long annealing times cause loss in crystallinity of the $MAPbBr_3$ thin film. Thus, we recommend a short annealing time for crystallization enhancement of sequential physical vapor deposited $MAPbBr_3$ thin films. In addition, Figure S1 shows that the $MAPbBr_3$ is be formed without post the annealing, indicating that the crystallization of the $MAPbBr_3$ starts within the chamber during the evaporation process. This is because the substrate temperature is 90˚C during the evaporation process of the MABr on $PbBr_2$, which is close to the annealing temperature (100˚C) for $MAPbBr_3$ reported previously [51]. Thus, the thermal energy is enough to heat the substrate, cause inter-diffusion and activate the reaction between $PbBr_2$ and MABr. Annealing at 100˚C for a short duration (10 mins) after the deposition is only required to enhance crystallization while preserving good crystallinity. Peaks corresponding to FTO were also observed and referenced by JCPDS card file number 41-1445.

X-ray line broadening is one of the characteristic features of XRD signatures and is measured from the full width half maximum (*FWHM*) of the diffraction peaks. It is basically due to three factors which include instrumental effects, crystallite size effect and micro-strains [52,53]. In our line broadening analysis, the instrumental effect is neglected because the same instrument is used so the same error is encountered for all samples. The effect of crystallite size and micro-strain cannot be separated hence we used the Williamson-Hall (W-H) plot to quantify their contributions to line broadening [54]. W-H analysis accounts for the contributions of crystallite size and micro-strain to peak broadening when large crystallites and thick films are involved. The *FWHM* for each $MAPbBr_3$ peak is determined from a Gaussian fit and used for the W-H analysis. Williamson and Hall formula is given by 2,

$$FWHM\cos\theta = \frac{K\lambda}{D} + 4\varepsilon\sin\theta \qquad 2$$

where D is the average crystallite size, λ is the wavelength, θ is the Bragg's diffraction angle, ε is the micro-strain, K is the Scherrer constant which is determined by the crystallite shape and is considered as 0.94 for spherical crystallites with cubic symmetry. The slope of the W-H plot ($FWHM\cos(\Theta)$ vs. $4\sin(\Theta)$) of the $MAPbBr_3$ diffractogram shown in Figure S7 (Supporting information) corresponds to the micro-strain and the crystallite size equals a constant multiplied by the reciprocal of the intercept. The negative slopes indicate negative micro-strains which may be due to compressive stress, stacking faults and the fact that strain is not the main cause of peak broadening. The effect of micro-strain cannot be ignored since it may originate from the thermal annealing and the minimization of interface, surface and grain boundary energies during grain growth. Compressive stresses are always found in films grown by PVD since the method is associated with particle bombardment [53]. The magnitude of the compressive micro-strain is observed to decrease as the thickness of MABr increases as shown in Figure S8. It is known that the magnitude of micro-strain is proportional to the degree of lattice distortion. The amount of lattice distortion can be measured from the change in a lattice constant from its bulk value. If the lattice constant of a thin film is smaller than its bulk value, then the strain is compressive in nature. The lattice constant of a cubic crystal structure is calculated using Bragg's law (Equation 3) and 4,

$$n\lambda = 2d\sin\theta \tag{3}$$

where $n = 1$ and d is the spacing between the planes of atoms.

$$a = d\left(h^2 + k^2 + l^2\right)^{\frac{1}{2}} \tag{4}$$

where a is the lattice constant and *(hkl)* are the miller indices. Figure 2b shows the variation of lattice constants of $MAPbBr_3$ thin film with MABr thickness. The lattice constant increases with increase in the thickness of MABr. In addition, the lattice constant of the 500 nm thick film (5.9240 Å) is closest to the lattice constant (5.9300(2) Å) of high-purity bulk $MAPbBr_3$ reported by *Tisdale et al.* [50], indicating that the unit cell is least distorted at 500 nm MABr thickness. Lattice distortion may be due to temperature differences (thermal expansion) and chemical differences (doping). The very small lattice distortion of the 500 nm thick MABr film may be due to very little chemical strain caused by small ionic radii differences of its constituents. Therefore, we can deduce that the phase purity increases with increase in MABr thickness. Figure 2c shows that increasing the thickness of MABr results in larger crystallites. The increase in average crystallite size and lattice constant with thickness of MABr may be caused by decrease in the magnitude of compressive micro-strain and could be responsible for the red shift in absorption onset that caused the narrowing of the band gap.

Dislocation density, ρ, is related to the crystallite size by Williamson and Smallman formula [55] given by 5,

$$\rho = \frac{n}{D^2} \tag{5}$$

where n equals unity for minimum dislocation density. Dislocation is a structural line defect which may be introduced during grain growth in the crystalline and is inversely proportional to the square of D. The dislocation density was observed to decrease from 2.891×10^{11} to 1.973×10^{11} cm^{-2} as the thickness of MABr is increased as shown by Figure 2d. *Hyder and Wilkov* [56] carried out an analytic study on the effect of dislocation density on the performance of InGaN based multi-junction solar cells. The observed that dislocation density has an adverse effect on Voc, Isc, PCE and the minority carrier lifetime. This implies that the film with 500 nm thickness of MABr, with the smallest dislocation defect density, may result in high performance solar cells.

Figures S2 and S3 (Supporting information) contain the XRD spectra of 200 nm $PbBr_2$:200 nm MABr, 100 nm $PbBr_2$:100 nm MABr and 200 nm $PbBr_2$:100 nm thin films. This is aimed at investigating the possibility of growing $MAPbBr_3$ thin film for equal thickness of $PbBr_2$ and MABr, and for thickness of $PbBr_2$ greater than that of MABr.

The intensity of the (100) diffraction plane is greater for the 100 nm $PbBr_2$:300 nm MABr than for 200 nm $PbBr_2$:200 nm MABr as shown in Figure S2 and the intensity for 200 nm $PbBr_2$:200 nm MABr is more that of 200 nm $PBBr_2$:100 nm MABr as shown in Figure S3. This shows that $MAPbBr_3$ thin films are more crystalline when the ratio of MABr to $PbBr_2$ is greater than unity. In particular, the intensity of the (100) and (200) peaks are very low for 200 nm $PbBr_2$:100 nm MABr, indicating that only a small proportion $MAPbBr_3$ phase is formed when the thickness of $PbBr_2$ is greater than that of MABr. This explains why our focus on optimizing the synthesis of $MAPbBr_3$ included only the variation of MABr thickness while that of $PbBr_2$ is kept constant.

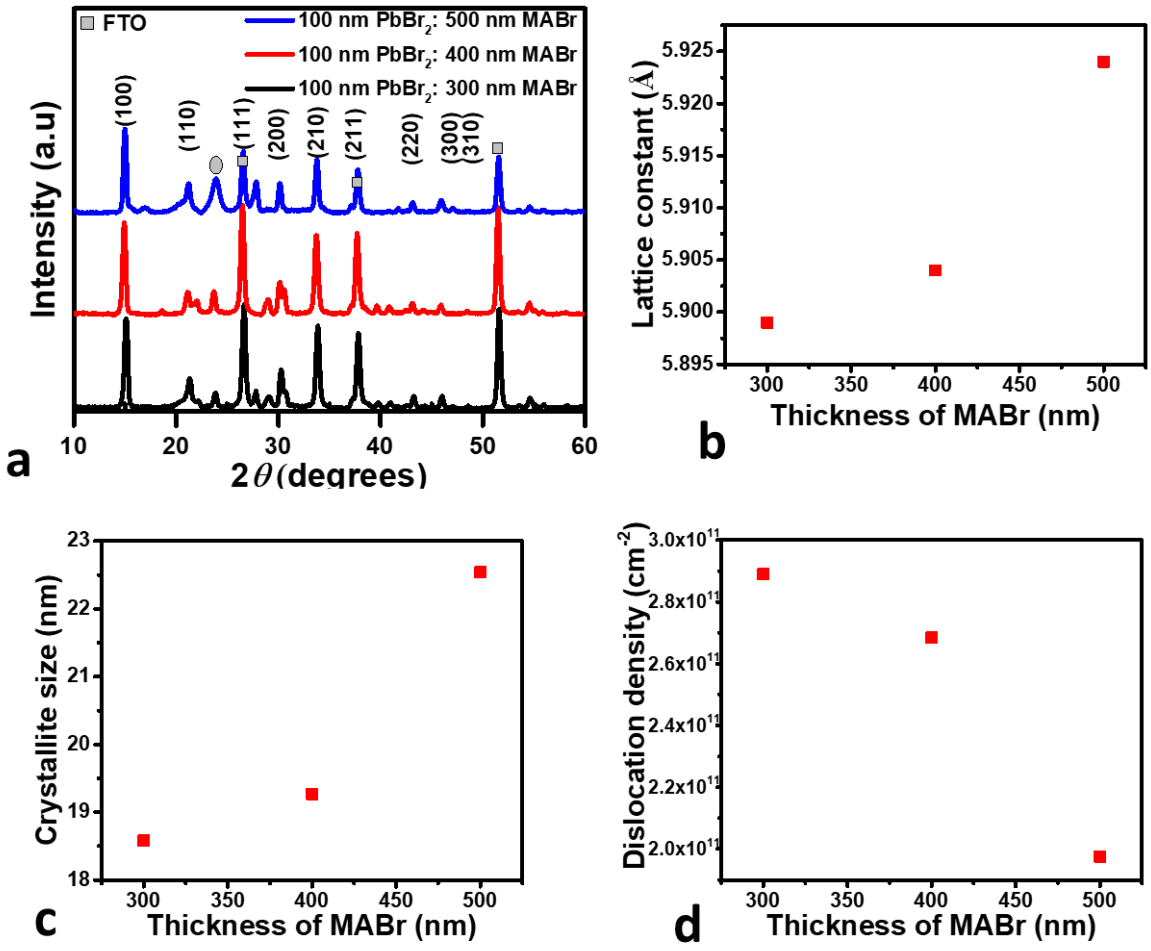

Figure 2: (a) XRD patterns of $MAPbBr_3$ for various thickness of MABr. (b) Change in lattice constant of $MAPbBr_3$ vs. thickness of MABr. film with thickness of MABr. (c) Change in crystallite size of $MAPbBr_3$ thin films vs. thickness of MABr. (d) Dislocation density of $MAPbBr_3$ thin film vs. thickness of MABr.

3.2 Morphological properties

Figure 3 represents the surface morphology of $MAPbBr_3$ thin films for various MABr thickness and variation of average grain size with thickness of MABr. All the samples showed pin-hole-free densely packed randomly distributed grains and full surface coverage as shown by Figure 3(a-c). The densely packed nature of the grains are important for solar cell applications because they minimize photo-current leakage [57]. *Eperon et al.* [57] showed that OIPs films with full coverage had the highest photocurrent which resulted in high PCE. The grain sizes and orientations were

also observed to vary indicating that films were polycrystalline. This crystallinity agrees with the sharp peaks observed on the XRD patterns with many diffraction planes. There is clear evidence of abnormal grain growth in which coarse grains are sandwiched by smaller grains. This is also an indication of the polycrystalline nature of the thin film, as explained by *Thompson* [58]. During grain growth in polycrystalline thin films, there is competition in minimizing surface, interface and strain energies, which leads differences in grain sizes and orientations [58,59]. The average grain size ranges from 217 to 302 nm and increases with the thickness of MABr as shown in Figure 3d. This is in agreement with *Dammers and Radelaar* [60] who showed that the size of columnar (faceted) grains of polycrystalline thin films, grown by vapour methods, is proportional to the square root of the film thickness. We think that the increase in average grain size with thickness of MABr may be due to decrease in the amount of $PbBr_2$ residue, as it reacts with the MABr leading to the formation of larger $MAPbBr_3$ grains. In addition, the increase in average grain size may be due to decrease in dislocation density which reduces abnormality in grain growth during thermal annealing [59]. This increase in average grain size is consistent with the increase in crystallite size discussed previously and is expected to cause decrease in grain boundaries and trap sites, leading to less electron scattering and nonradiative recombination during charge transport in solar cells. The average crystallite size obtained from W-H analysis is 10 times smaller than the grain size. This may be because polycrystalline thin film-grains consist of two or more crystallites which coalesce during grain growth as the film thickness is increased. *Garg et al*. [61] showed that the grain size of CsI equals its crystallite size when the thickness is less than 4 nm. As the film thickness is increased beyond 4 nm, the differences in grain and crystallite size increase because the crystallites move and merge to form bigger grains during the grain growth.

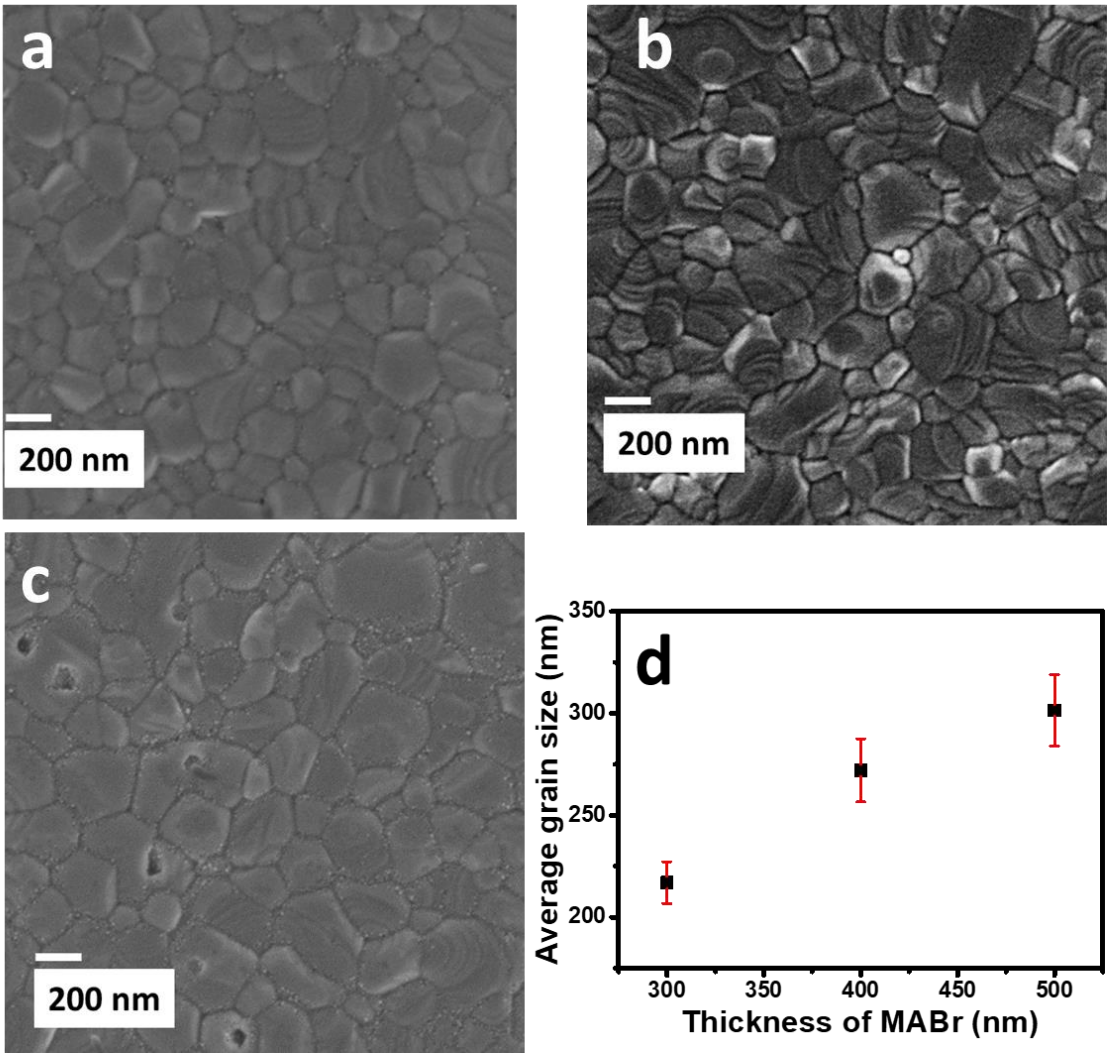

Figure 3: FE-SEM micrographs of $MAPbBr_3$ for various thickness. (a) 100 nm $PbBr_2$:300 nm MABr. (b) 100 nm $PbBr_2$:400 nm MABr. (c)100 nm $PbBr_2$:500 nm MABr. (d) Average grain size vs. thickness of MABr.

3.3 Optical properties

Figure 4a, b, c and d illustrate the UV-Vis absorption spectra of $MAPbBr_3$ thin films for various thicknesses, Tauc's plot of the absorption spectra, variation of band gap with lattice constant and thickness of the $MAPbBr_3$ for various thicknesses of MABr respectively. Each spectrum in Figure 4a shows a broad absorption band between 400 and 550 nm, in agreement with literature [62]. In addition, there is a red shift in absorption onset from 540 to 550 nm as the MABr thickness increased from 400 to 500 nm, corresponding to a decrease in band gap. The band gap was calculated using the *Mott and Davis* formula given in 6[63],

$$(\alpha h\upsilon)^{\frac{1}{n}} = A(h\upsilon - E_g) \qquad 6$$

where E_g is bandgap and A is a proportionality constant, where α is the absorption coefficient, h is the Planck's constant, υ is the frequency, n is a numerical constant and its value determines nature of the transition; n equals 1/2, 2, 3/2, and 3 for direct allowed transitions, indirect allowed transitions, direct forbidden transitions and indirect forbidden transitions respectively. The direct band gap Tauc-plots are shown in Figure 4b. The band gap decreases from 2.30 to 2.28 eV as the thickness of MABr increased. The decrease in band gap is due to increase in crystallite size as the thickness is MABr is increased. This inverse dependence of bandgap on the thickness is consistent with previous studies on CuI film [64] and may be attributed to the increase in crystallite size [65]. The narrowing bandgap may reduce the possibility of forming deep level traps leading decrease in carrier lifetime of solar cells [66]. Figure 4c shows that the band gap decreases as lattice constant increases, which agrees with previous reports for other semiconductors [67]. *Dalven* [67] showed by empirical calculations that the band gaps of cubic semiconductors are inversely proportional to the square of the lattice constant. This is because as the lattice constant increases the inter-atomic distance will increase. This causes the binding force between valence electrons and the parent atoms to decrease, thus requiring less energy to make them free (conduction) electrons. Figure 4d shows that the resulting film thickness is directly proportional to the thickness of MABr, however, it's less than the sum of the thickness of $PbBr_2$ and MABr. This may be due to bond formation during the reaction between $PbBr_2$ and MABr.

The effect of annealing time on optical properties was investigated and shown by Figure S3 (supporting information). It is observed that the band gap is independent of the annealing time, consistent with previous report on HPs by *Bi et al.* [68] . However, the absorbance increases slightly with increase in annealing time. In addition, the band gap of the unannealed film is equal to those of films annealed at 100 ℃ in air for various times. This confirms that the heat energy produced in the chamber was enough to cause interdiffusion and reaction between the $PbBr_2$ and MABr to produced $MAPbBr_3$. Therefore, further annealing for a short time (10 minutes) only helps to enhance further crystallization. Figures S4, S5 and S6 (Supporting information) show same absorption onset of 550 nm for the 500 nm MABr in three different experiments under similar conditions. This indicates that the method is repeatable and can be reproduced.

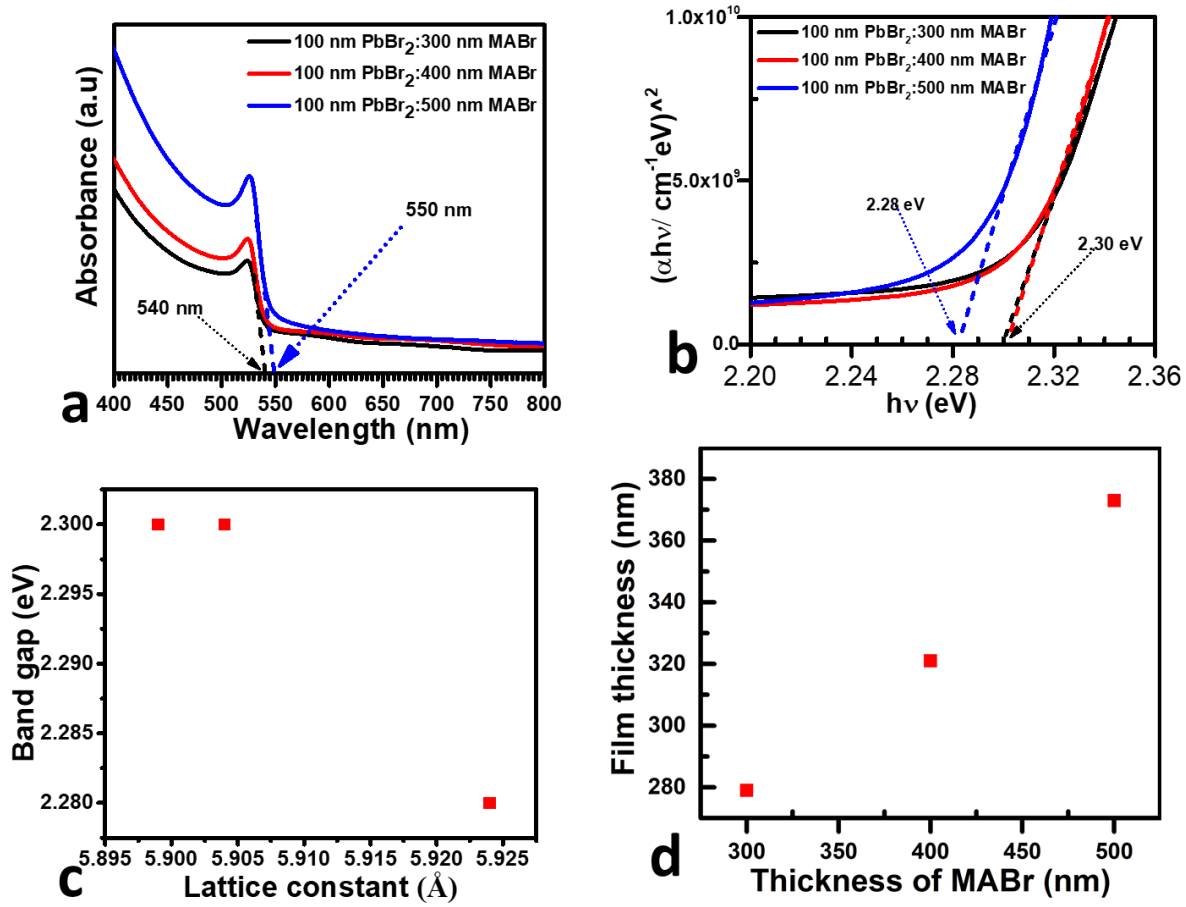

Figure 4: (a) UV-Vis absorption spectra of $MAPbBr_3$ for various thickness of MABr. (b) Direct bandgap Tauc-plot of $MAPbBr_3$ for various MABr thickness. (c) Band gap of $MAPbBr_3$ for various thickness of MABr. (d) The film thickness of $MAPbBr_3$ vs. thickness of MABr.

3.4 Electrical properties

3.4.1 Dark current-voltage analyses of Au/$MAPbBr_3$/FTO devices

Figure 5 shows the dark current-voltage (*I-V*) analyses of Au/$MAPbBr_3$/FTO devices for different thickness of MABr. In Figure 5a, a near-linear relationship between *I* and *V* is observed for the sample with 300 nm MABr thickness and a quadratic dependence as the thickness increased from 400 to 500 nm. These results are similar to those obtained for zero-bias Schottky detectors [69] and zero-bias Pt/$MaPbBr_3$/Au Schottky diode [70]. The semi-log *I-V* plots shown in Figure 5b are nearly symmetric [71], indicating slightly rectifying contacts. Since Au has a high work function of 5.1 eV [72], it forms an ohmic contact with a p-type material like $MAPbBr_3$, which has a work function of 4.6 eV [42]. This is because the barrier height, which corresponds to the difference between the functions of Au and $MAPbBr_3$ is small. The apparent slight rectification observed for the 400 and 500 nm MABr thick samples shown in Figure 5b may be due to the formation of a small barrier at the p-n junction between FTO (n-type) and $MAPbBr_3$. The ohmic contact facilitates the injection of electrons from the electrode into the bulk of $MAPbBr_3$ thin film. The quality of the ohmic contact is characterized by calculating the specific contact resistivity for the different devices. It is found to increase with the increase MABr thickness as shown in Figure 5d, indicating a decrease in the doping level

[73]. This implies that $MAPbBr_3$ thin film is self-doped and the level of doping decreases with increase the thickness of MABr. The bulk conduction mechanism was determined from the double-log *I-V* curves shown in Figure 5c. This was achieved by performing a linear fit of the graphs in order to determine the exponent of the general power law given by Equation 7 [71],

$$I = kV^m \tag{7}$$

where k is a constant and m the exponent, corresponding to the slope of the double-log *I-V* curve and determines the transport mechanism. If $m \sim 1$ then the bulk conduction is ohmic and dominated by thermally generated free charge carriers [71]. This implies that the density of the thermally generated free carriers is greater than the density of the injected carriers. On the other hand, if $m = 2$ then the trap-free space charge limited current (SCLC) mechanism is dominant. In this case, density of the injected carriers is greater than thermally generated charge carriers. Similarly, if m increases slowly to values slightly greater than two then shallow trap SCLC transport is dominant [74] and injected carriers go to fill the traps as the voltage is increased up to a limiting voltage V_{TFL}. This limiting voltage is known as the trap-filled limit and is the voltage for which all localized trap-states are filled, leading to a transition from ohmic to SCLC mechanism. For semiconductors with deep level traps, a very steep region exits on double-log *I-V* plot with slope that is far greater than 2 [75].

Our devices show double-log *I-V* characteristics with two distinct linear regions corresponding to the ohmic and shallow trap SCLC mechanisms as illustrated in Figure 5c. Only ohmic conduction is observed in the sample with 300 nm MABr thickness since $m \sim 1$ for all sections of the curve. The 400 and 500 nm MABr thick samples showed ohmic behaviour and SCLC bulk transport mechanism. Ohmic and SCLC mechanisms dominated in the 0 - 0.2 V and 0.7 – 1 V ranges respectively. No section of the curves had a steep slope confirming that only shallow traps are present in the $MAPbBr_3$. The shallow trap limited SCLC theory is then used to calculate charge carrier mobility, $\mu_{p,}$ and trap density, N_t. The N_t, is calculated using 8 [76],

$$V_{TFL} = qN_t \frac{d^2}{2\varepsilon_o \varepsilon_r} \tag{8}$$

where N_t is trap density, d is film thickness, q is electronic charge, ε_o is the vacuum permittivity, and ε_r the relative permittivity which is equal to 25.5 for $MAPbBr_3$ [76]. The calculated N_t decreased from 1.89 x 10^{16} to 1.40 x 10^{16} cm^{-3} as thickness increased from 400 to 500 nm, supporting the fact that dislocation density decreases with MABr thickness. These values are only one order of magnitude higher than the values obtained by Wenger et al. [77] for single crystal $MAPbBr_3$ thin films that gave rise to large diffusion length in micron. *Wenger et al*. [77] measured the N_t for single crystal $MAPbBr_3$ and thin films using light transmission spectroscopy, ellipsometry, spatially resolved and time-resolved photoluminescence spectroscopy and achieved 1.22 x 10^{15} and 7.0 x 10^{16} cm^{-3} respectively. Furthermore, our values had the same order of magnitude as those calculated for other OIPs that gave rise to high efficiency solar cells. *Yang et al*. [78] obtained trap density of 1.22 x 10^{16} cm^{-3} for $MAPbI_3$ perovskites which resulted in solar cells 19.62 % PCE. The $\mu_{p,}$ is calculated using the modified Mott-Gurney model [79] given in Equation 9. This equation is used to calculate μ_p in the presence of shallow traps located at discrete levels above the valence band.

$$J = \frac{9}{8}\varepsilon_o \varepsilon_r \theta \mu_p \frac{V^2}{d^3} \tag{9}$$

where d is film thickness, J is the current density, V is voltage at onset of space charge limited region, and θ is the trap factor, which is the ratio of free carriers to the sum of free and trapped carriers. It is calculated from the double-log I-V characteristics by dividing the current at the onset of the space charge region by the current at the end [79]. Our calculated μ_p from 1.89 x 10^{-2} to 1.08 x 10^{-1} cm^2 V^{-1} s^{-1} for 400 and 500 nm MABr thick samples respectively. These values are within the range of μ_p for inorganic semiconductors, 10^{-4} - 10^{3} cm^2 V^{-1} s^{-1} [80]. However, they are two orders of magnitude lower than values of μ_p for $MAPbBr_3$ single crystals obtained by the SCLC method. *Saidaminov et al*. [76] observed that the μ_p of high quality $MAPBBr_3$ single crystals prepared by inverse temperature crystallisation using the SCLC theory is 24 cm^2 V^{-1} s^{-1}. Using Mott-Gurney law, *Chen et al*. [81] obtained μ_p of 0.9, 5.6 and 54.6 cm^2 V^{-1} s^{-1} after the first, second and third crystallizations respectively, of bulk $MAPbBr_3$ crystals synthesized by inverse temperature crystallization. They attributed the increase in μ_p after repeated crystallization to be due formation of voids by surface states that favored the movement of electrons. The lower μ_p obtained for the polycrystalline thin films when compared with the single crystals may be due to the presence of ionized impurities at grain boundaries which scatter charge carriers, thus reducing their mobilities. Moreover, the μ_p was observed to increase proportionally with MABr thickness. This increase in μ_p may be due to the increase in grain size, which inevitably caused decrease in grain boundaries and trap density.

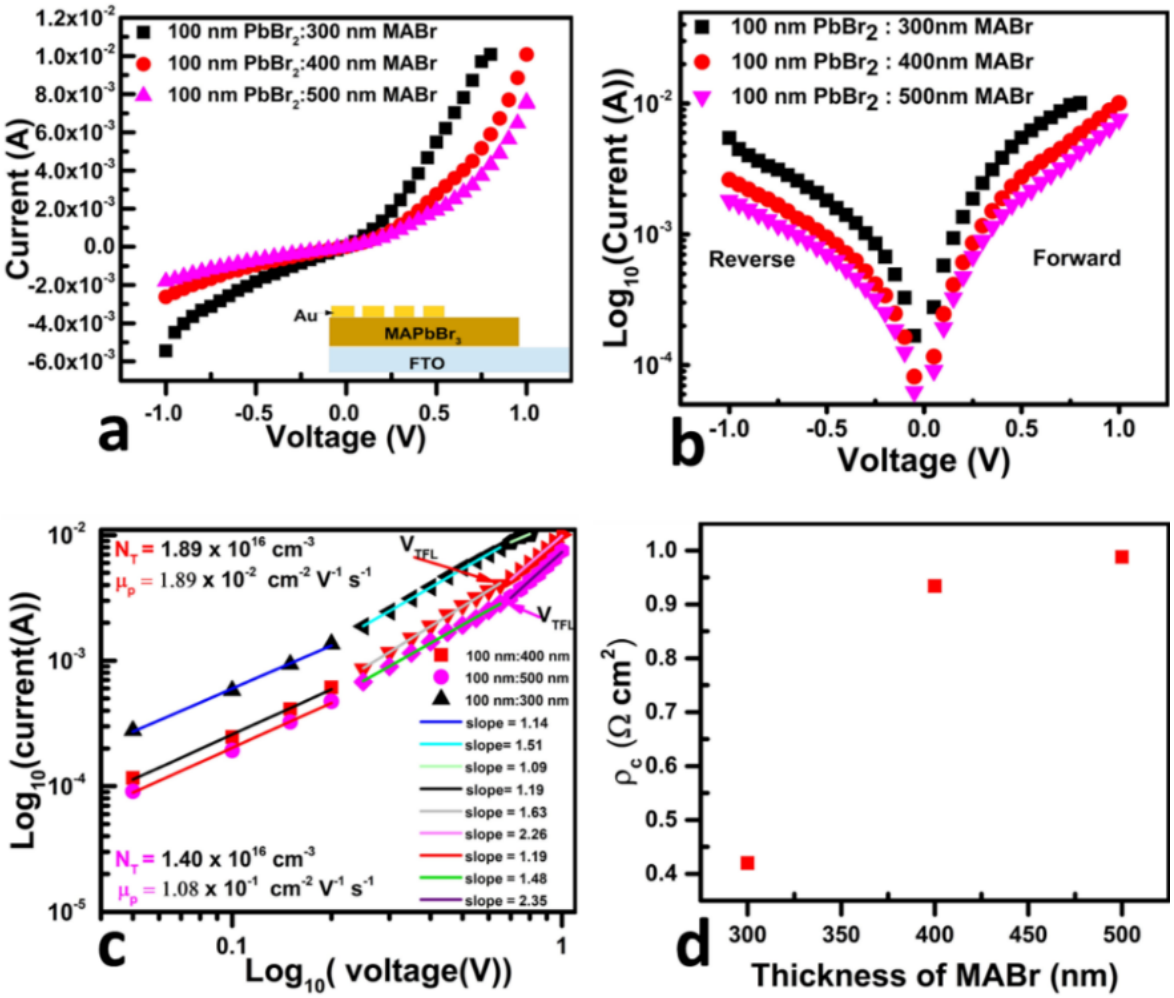

Figure 5: Electrical characterisation of FTO/MAPbBr3/Au. (a) I-V characteristic. (b) Semi-log I-V characteristics. (c) Double log I-V characteristics. (d) The specific resistivity of Au/MAPbBr$_3$/FTO vs. thickness of MABr.

3.4.2 Photoelectrical properties of Au/MAPbBr$_3$/FTO devices

Figure 6 represents the dark and light semi-log plots of the *I-V* characteristics of the Au/MAPbBr$_3$/FTO devices for different thicknesses of MABr. The intensity of the solar simulator was set to 100 mW/cm^2 and AM1.0 conditions. The switching from dark to light measurements was immediate. The light *I-V* characteristic is higher than the dark for any given bias indicating that the MAPbBr$_3$ is sensitive to visible light, in agreement with previous reports [82]. This is consistent with the UV-Vis spectra which shows absorption in the visible region of the electromagnetic spectrum. The greater current densities obtained under illumination is due to photogenerated charge carriers in the OIPs [83]. The generated electron-hole pairs are separated by the small electric field at the FTO/MAPbBr$_3$ n-p junction to constitute a current in the external circuit. The difference between the light and dark I-V characteristic is observed to increase with increase in the thickness of MABr as shown in Figure 6a, b and c indicating an increase in the photogenerated current. This may due to the decrease in band gap and increase in absorbance which leads to more photogenerated charge carriers. It may also be due to decrease in trap density, dislocation density and micro-strain which cause recombination of charge carriers. The curvature of the I-V reduces in the presence of light to almost linear relationships. This may be due reduction in the potential barrier due to the presence of ionic species as a result of light-induced ion migration [84].

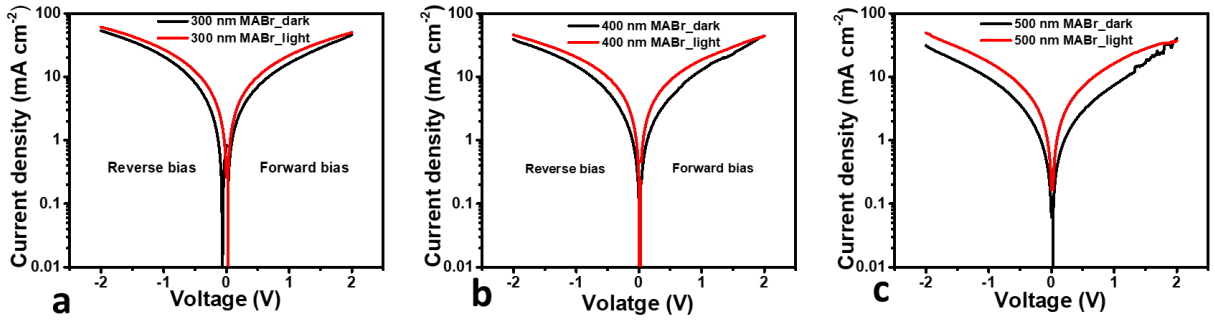

Figure 6: The I-V characteristics of Au/MAPbBr$_3$/FTO devices under light and dark conditions for different MABr thickness. (a) I-V characteristic of Au/MAPbBr$_3$/FTO devices containing 300 nm MABr. (b) I-V characteristic of Au/MAPbBr$_3$/FTO devices containing 400 nm MABr. (c) I-V characteristic of Au/MAPbBr$_3$/FTO devices containing 500 nm MABr.

4 Conclusion

MAPbBr$_3$ thin films were grown by SPVD of PbBr$_2$ and MABr single layers. The structural, morphological, optical, electrical and photoelectrical properties were found to depend greatly on the thickness of MABr. XRD diffractograms confirmed that all samples possessed the cubic crystal structure of MAPbBr$_3$ with $Pm\bar{3}m$ space group. In addition, the average crystallite size increased from 18.9 to 22.5 nm with increase in thickness of MABr. Furthermore, the micro-strain was compressive in nature and its magnitude decreased with increase in the thickness of MABr leading to increase in lattice constant and crystallite size. The lattice constant for the 500 nm MABr thick film was closest to the lattice constant of MAPbBr$_3$ singe crystal, synthesized from high purity precursors, indicating that its unit cell was the least distorted. FE-SEM micrographs showed large pin-hole-free densely packed grains that fully covered the substrate. The average grain size increased from 217 to 302 nm as the MABr the thickness of MABr was increased, indicating decrease in grain boundary. The average grain sizes were about ten times larger than the average crystallite sizes indicating that a grain consisted of many crystallites, which is consistent previous studies for thick polycrystalline thin films. UV-Vis absorption spectra showed broad absorption band ranging from 400 to 550 nm and a red shift in absorption onset from 540 to 550 nm due to increases in average crystallite size. Tauc-plot showed a minimum direct band gap of 2.28 eV for with 500 nm thick MABr. The band gap remained constant as the annealing time was increased from 0 to 60 minutes and the structure of as-deposited films confirmed the formation of highly crystalline MAPbBr$_3$

within the chamber, which implied that the thermal energy generated during evaporation was enough to activate the crystallization of the compound and only a short annealing time was therefore required to further enhance the reaction. Electrical properties revealed an increase in carrier mobility from 1.89 x 10^{-2} to 1.08 x 10^{-1} cm^2 V^{-1} s^{-1} and decrease in trap density from 1.89 x 10^{16} to 1.40 x 10^{16} cm^{-3} as MABr thickness increased. The specific contact resistivity of Au/$MAPbBr_3$/FTO devices increased with increase in the thickness of MABr indicating that $MAPbBr_3$ is self-doped and the level of doping decreased with increase in MABr thickness. Devices containing films with 500 nm MABr generated the highest photocurrent under 100 mW/cm^2 and AM1.0 illumination conditions due to high absorbance, small band gap and low defect density. In conclusion, the optimum properties for solar cell applications were achieved at 100 nm $PbBr_2$ and 500 nm of MABr, corresponding to resultant $MAPbBr_3$ film thickness of 373 nm. The same absorption onset (band gap) was obtained for three different experiments, indicating the method is repeatable. This method paves the way for stable and efficient PSCs.

Acknowledgements

The authors wish to thank the University of Pretoria, NRF-TWAS and NRF grant no N01156/115463 of the SARChI for financial support.

Supporting information

Eight Supporting Figures: XRD spectra of $PbBr_2$, MABr and $MAPbBr_3$ annealed at different times; XRD diffractograms of $MAPbBr_3$ including the spectrum of 200 nm PbBr:200 nm MABr ratio; XRD spectra for samples containing 200 nm $PbBr_2$:200 nm MABr, 100 nm $PbBr_2$:100 nm MABr and 200 nm $PbBr_2$:100 nm MABr thickness ratios; UV-Vis spectra of $MAPbBr_3$ including 500 nm thick MABr and annealed at different times; UV-Vis spectra of $MAPbBr_3$ for various thicknesses of MABr including 200 nm $PbBr_2$:200 nm MABr ratio; UV-Vis spectra of $MAPbBr_3$ for various thicknesses of MABr synthesized on glass; FWHMcos(Θ) vs. 4sin(Θ) for $MAPbBr_3$ film for different thicknesses of MABr; Micro-strain of $MAPbBr_3$ thin film vs. Thickness of MABr.

References

[1] A. Miyata, A. Mitioglu, P. Plochocka, O. Portugall, J.T.W. Wang, S.D. Stranks, H.J. Snaith, R.J. Nicholas, Direct measurement of the exciton binding energy and effective masses for charge carriers in organic-inorganic tri-halide perovskites, Nat. Phys. 11 (2015) 582–587. doi:10.1038/nphys3357.

[2] Q. Dong, Y. Fang, Y. Shao, J. Qiu, L. Cao, J. Huang, Electron-hole diffusion lengths > 175 μm in solution-grown CH 3 NH 3 PbI 3 single, (2015) 1–8.

[3] Y. Lee, J. Kwon, E. Hwang, C.H. Ra, W.J. Yoo, J.H. Ahn, J.H. Park, J.H. Cho, High-performance perovskite-graphene hybrid photodetector, Adv. Mater. 27 (2015) 41–46. doi:10.1002/adma.201402271.

[4] L. Wang, G.D. Yuan, R.F. Duan, F. Huang, T.B. Wei, Z.Q. Liu, J.X. Wang, J.M. Li, Tunable bandgap in hybrid perovskite CH3NH3Pb (Br3-yXy) single crystals and photodetector applications Tunable bandgap in hybrid perovskite CH 3 NH 3 Pb (Br 3 − y X y) single crystals and photodetector applications, 045115 (2016). doi:10.1063/1.4948312.

[5] H. Tsai, R. Asadpour, J. Blancon, C.C. Stoumpos, O. Durand, J.W. Strzalka, B. Chen, R. Verduzco, P.M. Ajayan, S. Tretiak, J. Even, M.A. Alam, M.G. Kanatzidis, W. Nie, A.D. Mohite, Light-induced lattice expansion leads to high-efficiency perovskite solar cells, 70 (2018) 67–70.

[6] Q. Wang, Y. Shao, H. Xie, L. Lyu, X. Liu, Y. Gao, J. Huang, Qualifying composition dependent p and n self-doping in CH3NH3PbI3, Appl. Phys. Lett. 105 (2014). doi:10.1063/1.4899051.

[7] Z. Yu, L. Sun, Recent Progress on Hole-Transporting Materials for Emerging Organometal Halide Perovskite Solar Cells, (2015). doi:10.1002/aenm.201500213.

[8] T. Kirchartz, T. Markvart, U. Rau, D.A. Egger, Impact of Small Phonon Energies on the Charge- Carrier Lifetimes in Metal-Halide Perovskites Impact of Small Phonon Energies on the Charge-Carrier Lifetimes in Metal-Halide Perovskites, (2018). doi:10.1021/acs.jpclett.7b03414.

[9] S.S. Mali, C.S. Shim, C.K. Hong, Highly stable and efficient solid-state solar cells based on methylammonium lead bromide (CH3NH3PbBr3) perovskite quantum dots, NPG Asia Mater. 7 (2015) e208-9. doi:10.1038/am.2015.86.

[10] J.E. Bishop, J.A. Smith, C. Greenland, V. Kumar, N. Vaenas, O.S. Game, T.J. Routledge, M. Wong-Stringer, C. Rodenburg, D.G. Lidzey, High-Efficiency Spray-Coated Perovskite Solar Cells Utilizing Vacuum-Assisted Solution Processing, ACS Appl. Mater. Interfaces. 10 (2018) 39428–39434. doi:10.1021/acsami.8b14859.

[11] R. Singh, I.M. Noor, P.K. Singh, B. Bhattacharya, A.K. Arof, Synthesis of active absorber layer by dip-coating method for perovskite solar cell, J. Mol. Struct. 1158 (2018) 229–233. doi:10.1016/j.molstruc.2018.01.037.

[12] P. Fan, D. Gu, G.X. Liang, J.T. Luo, J.L. Chen, Z.H. Zheng, D.P. Zhang, High-performance perovskite CH3NH3PbI3thin films for solar cells prepared by single-source physical vapour deposition, Sci. Rep. 6 (2016) 1–9. doi:10.1038/srep29910.

[13] P. Luo, S. Zhou, W. Xia, J. Cheng, C. Xu, Y. Lu, Chemical Vapor Deposition of Perovskites for Photovoltaic Application, Adv. Mater. Interfaces. 4 (2017). doi:10.1002/admi.201600970.

[14] S. Bonomi, D. Marongiu, N. Sestu, M. Saba, M. Patrini, G. Bongiovanni, L. Malavasi, Novel Physical Vapor Deposition Approach to Hybrid Perovskites: Growth of MAPbI3 Thin Films by RF-Magnetron Sputtering, Sci. Rep. 8 (2018) 1–19. doi:10.1038/s41598-018-33760-w.

[15] D. Richmond, M. McCormick, T.K. Ekanayaka, J.D. Teeter, B.L. Swanson, N. Benker, G. Hao, S. Sikich, A. Enders, A. Sinitskii, C.C. Ilie, P.A. Dowben, A.J. Yost, Inkjet Printing All Inorganic Halide Perovskite Inks for Photovoltaic Applications, J. Vis. Exp. (2019) 1–10. doi:10.3791/58760.

[16] J.H. Huang, K.J. Jiang, X.P. Cui, Q.Q. Zhang, M. Gao, M.J. Su, L.M. Yang, Y. Song, Direct Conversion of CH 3 NH 3 PbI 3 from Electrodeposited PbO for Highly Efficient Planar Perovskite Solar Cells, Sci. Rep. 5 (2015) 1–8. doi:10.1038/srep15889.

[17] N.K. Noel, B. Wenger, S.N. Habisreutinger, J.B. Patel, T. Crothers, Z. Wang, R.J. Nicholas, M.B. Johnston, L.M. Herz, H.J. Snaith, Highly Crystalline Methylammonium Lead Tribromide Perovskite Films for Efficient Photovoltaic Devices, ACS Energy Lett. 3 (2018) 1233–1240. doi:10.1021/acsenergylett.8b00509.

[18] D.H. Jung, J.H. Park, H.E. Lee, J. Byun, T.H. Im, G.Y. Lee, J.Y. Seok, T. Yun, K.J. Lee, S.O. Kim, Flash-induced ultrafast recrystallization of perovskite for flexible light-emitting diodes, Nano Energy. (2019). doi:10.1016/j.nanoen.2019.04.061.

[19] K. Wang, S. Wang, S. Xiao, Q. Song, Recent Advances in Perovskite Micro- and Nanolasers, Adv. Opt. Mater. 6 (2018) 1–27. doi:10.1002/adom.201800278.

[20] F. Bertocci, A. Fort, V. Vignoli, M. Mugnaini, R. Berni, Optimization of perovskite gas sensor performance: characterization, measurement and experimental design, Sensors (Switzerland). 17 (2017). doi:10.3390/s17061352.

[21] S. Ahmad, C. George, D.J. Beesley, J.J. Baumberg, M. De Volder, Photo-Rechargeable Organo-Halide Perovskite Batteries, Nano Lett. 18 (2018) 1856–1862. doi:10.1021/acs.nanolett.7b05153.

[22] Z. Xu, Z. Liu, Y. Huang, G. Zheng, Q. Chen, H. Zhou, To probe the performance of perovskite memory devices: Defects property and hysteresis, J. Mater. Chem. C. 5 (2017) 5810–5817. doi:10.1039/c7tc00266a.

[23] M. Zhang, F. Zhang, Y. Wang, L. Zhu, Y. Hu, Z. Lou, Y. Hou, F. Teng, High-Performance Photodiode-Type Photodetectors Based on Polycrystalline Formamidinium Lead Iodide Perovskite Thin Films, Sci. Rep. 8 (2018) 1–9. doi:10.1038/s41598-018-29147-6.

[24] A. Kojima, K. Teshima, Y. Shirai, T. Miyasaka, Organometal Halide Perovskites as Visible-Light Sensitizers for Photovoltaic, (2009) 6050–6051.

[25] A. Kumar Jena, A. Kulkarni, T. Miyasaka, Halide Perovskite Photovoltaics: Background, Status, and Future Prospects, Chem. Rev. (2018). doi:10.1021/acs.chemrev.8b00539.

[26] M.A. Green, Y. Hishikawa, E.D. Dunlop, D.H. Levi, J. Hohl-Ebinger, M. Yoshita, A.W.Y. Ho-Baillie, Solar cell efficiency tables (Version 53), Prog. Photovoltaics Res. Appl. 27 (2019) 3–12. doi:10.1002/pip.3102.

[27] Q. Wang, N. Phung, D. Di Girolamo, P. Vivo, A. Abate, Enhancement in lifespan of halide perovskite solar cells, Energy Environ. Sci. 12 (2018) 865–886. doi:10.1039/c8ee02852d.

[28] M. Malekshahi, A. Nemati, N. Taghavinia, Moisture stability in nanostructured perovskite solar cells, Mater. Lett. 237 (2019) 356–360. doi:10.1016/j.matlet.2018.10.029.

[29] A.D. Sheikh, R. Munir, M.A. Haque, A. Bera, W. Hu, P. Shaikh, A. Amassian, T. Wu, Effects of High Temperature and Thermal Cycling on the Performance of Perovskite Solar Cells: Acceleration of Charge Recombination and Deterioration of Charge Extraction, ACS Appl. Mater. Interfaces. 9 (2017) 35018–35029. doi:10.1021/acsami.7b11250.

[30] Y. Sun, X. Fang, Z. Ma, L. Xu, Y. Lu, Q. Yu, N. Yuan, J. Ding, Enhanced UV-light stability of organometal halide perovskite solar cells with interface modification and a UV absorption layer, J. Mater. Chem. C. 5 (2017) 8682–8687. doi:10.1039/c7tc02603j.

[31] K. Qin, B. Dong, S. Wang, Improving the stability of metal halide perovskite solar cells from material to structure, J. Energy Chem. 33 (2019) 90–99. doi:10.1016/j.jechem.2018.08.004.

[32] W. Ming, D. Yang, T. Li, L. Zhang, M. Du, Formation and Diffusion of Metal Impurities in Perovskite Solar Cell Material CH 3 NH 3 PbI 3 : Implications on Solar Cell Degradation and Choice of Electrode, (2018). doi:10.1002/advs.201700662.

[33] S. Sidhik, A.C. Pasarán, C. Rosiles Pérez, T. López-Luke, E. De La Rosa, Modulating the grain size, phase and optoelectronic quality of perovskite films with cesium iodide for high-performance solar cells, J. Mater. Chem. C. 6 (2018) 7880–7889. doi:10.1039/c8tc02923g.

[34] W.L. Schmidt, K. Tsevas, B. Ozkan, C.M. Handley, C.L. Freeman, D.C. Sinclair, I.M. Reaney, W.C. Tsoi, C. Rodenburg, Materials Chemistry A, (2018) 23578–23586. doi:10.1039/c8ta08231f.

[35] R. Wang, M. Mujahid, Y. Duan, Z.K. Wang, J. Xue, Y. Yang, A Review of Perovskites Solar Cell Stability, Adv. Funct. Mater. 1808843 (2019) 1–25. doi:10.1002/adfm.201808843.

[36] C.C. Boyd, R. Cheacharoen, T. Leijtens, M.D. Mcgehee, Understanding Degradation Mechanisms and Improving Stability of Perovskite Photovoltaics, Chem. Rev. 119 (2018) 3418–3451. doi:10.1021/acs.chemrev.8b00336.

[37] R. Yang, L. Zhang, Y. Cao, Y. Miao, Y. Ke, Y. Wei, Q. Guo, Inhomogeneous degradation in metal halide perovskites, 111 (2017).

[38] Z. Yu, Y. Shao, J.E. Shield, J. Zhao, X. Zheng, Y. Deng, J. Huang, H. Wei, Strained hybrid perovskite thin films and their impact on the intrinsic stability of perovskite solar cells, Sci. Adv. 3 (2017) eaao5616. doi:10.1126/sciadv.aao5616.

[39] P. Zhang, F. Yang, G. Kapil, C.H. Ng, T. Ma, S. Hayase, Preparation of Perovskite Films under Liquid Nitrogen Atmosphere for High Efficiency Perovskite Solar Cells, ACS Sustain. Chem. Eng. (2019).

doi:10.1021/acssuschemeng.8b05139.

[40] R. Sheng, A. Ho-baillie, S. Huang, S. Chen, X. Wen, X. Hao, M.A. Green, Methylammonium Lead Bromide Perovskite-Based Solar Cells by Vapor-Assisted Deposition, (2015). doi:10.1021/jp512936z.

[41] A. Rolland, L. Pedesseau, M. Kepenekian, C. Katan, Y. Huang, S. Wang, C. Cornet, O. Durand, J. Even, Computational analysis of hybrid perovskite on silicon 2-T tandem solar cells based on a Si tunnel junction, Opt. Quantum Electron. 50 (2018). doi:10.1007/s11082-017-1284-0.

[42] M.R. Leyden, L. Meng, Y. Jiang, L.K. Ono, L. Qiu, E.J. Juarez-perez, C. Qin, C. Adachi, Y. Qi, Methylammonium Lead Bromide Perovskite Light-Emitting Diodes by Chemical Vapor Deposition, (2017). doi:10.1021/acs.jpclett.7b01093.

[43] M. Jäckle, H. Linnenbank, M. Hentschel, M. Saliba, S.G. Tikhodeev, H. Giessen, Tunable green lasing from circular grating distributed feedback based on $CH_3NH_3PbBr_3$ perovskite, Opt. Mater. Express. 9 (2019) 2006. doi:10.1364/OME.9.002006.

[44] J. Ávila, C. Momblona, P.P. Boix, M. Sessolo, H.J. Bolink, Vapor-Deposited Perovskites: The Route to High-Performance Solar Cell Production?, Joule. 1 (2017) 431–442. doi:10.1016/j.joule.2017.07.014.

[45] L.K. Ono, M.R. Leyden, S. Wang, Y. Qi, Organometal halide perovskite thin films and solar cells by vapor deposition, J. Mater. Chem. A. 4 (2016) 6693–6713. doi:10.1039/c5ta08963h.

[46] P. Pistor, J. Borchert, W. Fränzel, R. Csuk, R. Scheer, Monitoring the phase formation of coevaporated lead halide perovskite thin films by in situ x-ray diffraction, J. Phys. Chem. Lett. 5 (2014) 3308–3312. doi:10.1021/jz5017312.

[47] M.C. Jung, S.R. Raga, Y. Qi, Properties and solar cell applications of Pb-free perovskite films formed by vapor deposition, RSC Adv. 6 (2016) 2819–2825. doi:10.1039/c5ra21291j.

[48] K.H. Wang, L.C. Li, M. Shellaiah, K.W. Sun, Structural and Photophysical Properties of Methylammonium Lead Tribromide (MAPbBr 3) Single Crystals, Sci. Rep. 7 (2017) 1–14. doi:10.1038/s41598-017-13571-1.

[49] W. Peng, L. Wang, B. Murali, K. Ho, A. Bera, N. Cho, C. Kang, V.M. Burlakov, J. Pan, L. Sinatra, C. Ma, W. Xu, D. Shi, E. Alarousu, A. Goriely, J. He, O.F. Mohammed, T. Wu, O.M. Bakr, Solution-Grown Monocrystalline Hybrid Perovskite Films for Hole-Transporter-Free Solar Cells, (2016) 3383–3390. doi:10.1002/adma.201506292.

[50] J.T. Tisdale, T. Smith, J.R. Salasin, M. Ahmadi, N. Johnson, A. V. Ievlev, M. Koehler, C.J. Rawn, E. Lukosi, B. Hu, Precursor purity effects on solution-based growth of MAPbBr 3 single crystals towards efficient radiation sensing, CrystEngComm. 20 (2018) 7818–7825. doi:10.1039/c8ce01498a.

[51] M. Jäckle, H. Linnenbank, M. Hentschel, M. Saliba, S.G. Tikhodeev, H. Giessen, Tunable green lasing from circular grating distributed feedback based on CH 3 NH 3 PbBr 3 perovskite , Opt. Mater. Express. 9 (2019) 2006. doi:10.1364/ome.9.002006.

[52] P.M. Shafi, A.C. Bose, Impact of crystalline defects and size on X-ray line broadening : A phenomenological approach for tetragonal SnO2 nanocrystals Impact of crystalline defects and size on X-ray line broadening : A phenomenological approach for tetragonal, 057137 (2015). doi:10.1063/1.4921452.

[53] A.R. Bushroa, R.G. Rahbari, H.H. Masjuki, M.R. Muhamad, Approximation of crystallite size and microstrain via XRD line broadening analysis in TiSiN thin fi lms, Vaccum. 86 (2012) 1107–1112. doi:10.1016/j.vacuum.2011.10.011.

[54] G.K. Williamson, W.H. Hall, X-ray line broadening from filed aluminium and wolframL'elargissement des raies de rayons x obtenues des limailles d'aluminium et de tungsteneDie verbreiterung der roentgeninterferenzlinien von aluminium- und wolframspaenen, Acta Metall. 1 (1953) 22–31.

doi:https://doi.org/10.1016/0001-6160(53)90006-6.

[55] G.K. Williamson, R.E. Smallman, III. Dislocation densities in some annealed and cold-worked metals from measurements on the X-ray Debye-Scherrer spectrum, Philos. Mag. 1 (1956) 34–46. doi:10.1080/14786435608238074.

[56] S.B. Hyder, M.A. Wilkov, Effect of dislocation density on the epitaxial growth of silver, J. Appl. Phys. 38 (1967) 2386–2387. doi:10.1063/1.1709890.

[57] Giles E. Eperon, Victor M. Burlakov, Pablo Docampo, Alain Goriely, Henry J. Snaith, Morphological Control for High Performance, Solution-Processed Planar Heterojunction Perovskite Solar Cells, Adv. Funct. Mater. (2013) 151–157. doi:10.1002/adfm.201302090.

[58] C. V. Thompson, Grain growth in polycrystalline thin films of semiconductors, Interface Sci. 6 (1998) 85–93.

[59] D.N. Lee, H.Y.O.J. Lee, Effect of Stresses on the Evolution of Annealing Textures in Cu and Al Interconnects, 32 (2003).

[60] A.J. Dammers, S. Radelaar, Two-Dimensional Computer Modelling of Polycrystalline Film Growth, Textures Microstruct. 14 (1991) 757–762. doi:10.1155/tsm.14-18.757.

[61] P. Garg, R. Rai, B.K. Singh, Nuclear Instruments and Methods in Physics Research A Structural characterization of " as-deposited " cesium iodide fi lms studied by X-ray diffraction and transmission electron microscopy techniques, Nucl. Inst. Methods Phys. Res. A. 736 (2014) 128–134. doi:10.1016/j.nima.2013.10.075.

[62] A. Mhamdi, H. Mehdi, A. Bouazizi, G. Garcia-Belmonte, One-step methylammonium lead bromide films: Effect of annealing treatment, J. Mol. Struct. 1192 (2019) 1–6. doi:10.1016/j.molstruc.2019.04.113.

[63] E.A. Davis, N.F. Mott, Conduction in non-crystalline systems V. Conductivity, optical absorption and photoconductivity in amorphous semiconductors, Philos. Mag. 22 (1970) 903–922. doi:10.1080/14786437008221061.

[64] N.M. Gosavi, A.R. Shelke, N.G. Deshpande, S.R. Gosavi, A.M. Patil, C.P. Sawant, A.D. Dhondge, Influence of Thickness on the Photosensing Properties of Chemically Synthesized Copper Sulfide Thin Films, World J. Condens. Matter Phys. 05 (2015) 1–9. doi:10.4236/wjcmp.2015.51001.

[65] M. Singh, M. Goyal, K. Devlal, Size and shape effects on the band gap of semiconductor compound nanomaterials, J. Taibah Univ. Sci. 12 (2018) 470–475. doi:10.1080/16583655.2018.1473946.

[66] L. Kong, G. Liu, J. Gong, Q. Hu, R.D. Schaller, P. Dera, D. Zhang, Z. Liu, W. Yang, K. Zhu, Y. Tang, C. Wang, S.-H. Wei, T. Xu, H. Mao, Simultaneous band-gap narrowing and carrier-lifetime prolongation of organic–inorganic trihalide perovskites, Proc. Natl. Acad. Sci. 113 (2016) 8910–8915. doi:10.1073/pnas.1609030113.

[67] R. Dalven, Empirical relation between energy gap and lattice constant in cubic semiconductors, Phys. Rev. B. 8 (1973) 6033–6034. doi:10.1103/PhysRevB.8.6033.

[68] C. Bi, Y. Shao, Y. Yuan, Z. Xiao, C. Wang, Understanding the formation and evolution of interdi ff usion grown organolead halide perovskite thin fi lms by thermal annealing †, (2014) 18508–18514. doi:10.1039/c4ta04007d.

[69] J.L. Hesler, T.W. Crowe, V. Diodes, Responsivity and noise measurements of zero-bias Schottky diode detectors, 18th Int. Symp. Sp. Terahertz Technol. (2007) 89.

[70] P.A. Shaikh, D. Shi, J.R.D. Retamal, A.D. Sheikh, M.A. Haque, C.F. Kang, J.H. He, O.M. Bakr, T. Wu, Schottky junctions on perovskite single crystals: Light-modulated dielectric constant and self-biased

photodetection, J. Mater. Chem. C. 4 (2016) 8304–8312. doi:10.1039/c6tc02828d.

[71] A. Hajibadali, M.B. Nejad, G. Farzi, Schottky Diodes Based on Polyaniline / Multi-Walled Carbon Nanotube Composites, (2015). doi:10.1007/s13538-015-0334-y.

[72] M. DeJarld, P.M. Campbell, A.L. Friedman, M. Currie, R.L. Myers-Ward, A.K. Boyd, S.G. Rosenberg, S.P. Pavunny, K.M. Daniels, D.K. Gaskill, Surface potential and thin film quality of low work function metals on epitaxial graphene, Sci. Rep. 8 (2018) 1–11. doi:10.1038/s41598-018-34595-1.

[73] S. Gupta, P. Paramahans Manik, R. Kesh Mishra, A. Nainani, M.C. Abraham, S. Lodha, Contact resistivity reduction through interfacial layer doping in metal-interfacial layer-semiconductor contacts, J. Appl. Phys. 113 (2013). doi:10.1063/1.4811340.

[74] P. Ca, I. Chakraborty, N. Panwar, A. Khanna, U. Ganguly, Space Charge Limited Current with Self-heating in, 1 (n.d.).

[75] T. Kirchartz, Influence of diffusion on space-charge-limited current measurements in organic semiconductors, Beilstein J. Nanotechnol. 4 (2013) 180–188. doi:10.3762/bjnano.4.18.

[76] M.I. Saidaminov, A.L. Abdelhady, B. Murali, E. Alarousu, V.M. Burlakov, W. Peng, I. Dursun, L. Wang, Y. He, G. MacUlan, A. Goriely, T. Wu, O.F. Mohammed, O.M. Bakr, High-quality bulk hybrid perovskite single crystals within minutes by inverse temperature crystallization, Nat. Commun. 6 (2015) 1–6. doi:10.1038/ncomms8586.

[77] B. Wenger, P.K. Nayak, X. Wen, S. V. Kesava, N.K. Noel, H.J. Snaith, Consolidation of the optoelectronic properties of CH3NH3PbBr3 perovskite single crystals, Nat. Commun. 8 (2017). doi:10.1038/s41467-017-00567-8.

[78] D. Yang, X. Zhou, R. Yang, Z. Yang, W. Yu, X. Wang, C. Li, S. Liu, R.P.H. Chang, Surface optimization to eliminate hysteresis for record efficiency planar perovskite solar cells, Energy Environ. Sci. 9 (2016) 3071–3078. doi:10.1039/c6ee02139e.

[79] S.A. Moiz, M.M. Ahmed, K.S. Karimov, Estimation of electrical parameters of OD organic semiconductor diode from measured I-V characteristics, ETRI J. 27 (2005) 319–324. doi:10.4218/etrij.05.0104.0100.

[80] G.F. Yu, M. Yu, W. Pan, W.P. Han, X. Yan, J.C. Zhang, H. Di Zhang, Y.Z. Long, Electrical transport properties of an isolated CdS microrope composed of twisted nanowires, Nanoscale Res. Lett. 10 (2015) 1–7. doi:10.1186/s11671-015-0734-5.

[81] L.C. Chen, K.L. Lee, S.E. Lin, Observation of hybrid MAPBBr3 perovskite bulk crystals grown by repeated crystallizations, Crystals. 8 (2018). doi:10.3390/cryst8070260.

[82] N. Yi, S. Wang, Z. Duan, K. Wang, Q. Song, S. Xiao, Tailoring the Performances of Lead Halide Perovskite Devices with Electron-Beam Irradiation, Adv. Mater. 29 (2017) 1–8. doi:10.1002/adma.201701636.

[83] C. Ozaydin, Electrical and Photoelectrical Properties of Copper (II) Complex/n-Si/Au Heterojunction Diode, Am. J. Opt. Photonics. 2 (2014) 69. doi:10.11648/j.ajop.20140206.11.

[84] J.F. Galisteo-López, Y. Li, H. Míguez, Three-Dimensional Optical Tomography and Correlated Elemental Analysis of Hybrid Perovskite Microstructures: An Insight into Defect-Related Lattice Distortion and Photoinduced Ion Migration, J. Phys. Chem. Lett. 7 (2016) 5227–5234. doi:10.1021/acs.jpclett.6b02456.